Boosting photocatalytic oxidation on graphitic carbon nitride for efficient photocatalysis by heterojunction with graphitic carbon units

Hassan R.S. Abdellatif, Guan Zhang, Xiaotian Wang, DetiXie, John T.S. Irvine, Jiupai Ni, Chengsheng Ni

PII: S1385-8947(19)30738-7
DOI: https://doi.org/10.1016/j.cej.2019.03.266
Reference: CEJ 21390

To appear in: *Chemical Engineering Journal*

Received Date: 26 December 2018
Revised Date: 3 March 2019
Accepted Date: 28 March 2019

Please cite this article as: H.R.S. Abdellatif, G. Zhang, X. Wang, DetiXie, J.T.S. Irvine, J. Ni, C. Ni, Boosting photocatalytic oxidation on graphitic carbon nitride for efficient photocatalysis by heterojunction with graphitic carbon units, *Chemical Engineering Journal* (2019), doi: https://doi.org/10.1016/j.cej.2019.03.266

Boosting photocatalytic oxidation on graphitic carbon nitride for efficient photocatalysis by heterojunction with graphitic carbon units

Hassan R. S. Abdellatif[a], Guan Zhang[b], Xiaotian Wang[c], DetiXie[a], John T.S. Irvine [d], Jiupai Ni[a]* and Chengsheng Ni[a]*

[a]College of Resources and Environment, Southwest University, Chongqing 400716, China

[b]School of Civil and Environmental Engineering, Harbin Institute of Technology, Shenzhen, Shenzhen 518055, P. R. China

[c]School of Physical Science and Technology, Southwest University, Chongqing 400716, China

[d]School of Chemistry, University of St Andrews, Fife, KY16 9ST, Scotland, UK

*Corresponding authors: J.N. nijiupai@163.com, C. N. nichengsheg@163.com; nichengsheg@swu.edu.cn.

Supporting information is available online.

Abstract

Graphitic carbon nitride has been considered as a promising metal-free visible light photocatalyst for air pollutants oxidation due to its suitable band-gap energy and higher conduction band edge. Herein, we have developed a facile approach for dramatically downwards shifting band edge positions of carbon nitride up by about 1 eV *via* in-plane heterojunction with graphitic carbon units to enhance the oxidation capability of the electron holes generated from the valence band. The graphitic carbon units in junction with tri-s-triazine domains were clearly observed and its in-plane hybridization with carbon nitride was formed during the copolymerization using melamine with a small amount of m-phenylenediamine as the precursors. The direct intralayer junction between the tri-s-triazine and the graphitic carbon domain, essentially different with interlayer junction reported in literature, is able to shift downwards the band edge positions via merging electron density of states of carbon nitride with that of graphitic carbon, and thus would be beneficial for separation of photoexcited charge carriers and generation of hydroxyl radicals for the oxidation of pollutants. The hybrid photocatalyst prepared with a small quantity (less than 1%) of m-phenylenediamine and melamine as precursors has shown much enhanced NO oxidation to final products(NO_2^- and NO_3^-) and increased NO removal 10% than the one from melamine only.

Introduction

Nowadays, air pollution has become one of the biggest challenges due to the development of the economy and industry leads to the increasing demand for conventional fuels[1]. Nitric oxide (NO) is a major air pollutant derived from combustion of fossil fuels and vehicles exhaust[2, 3], and rather it is one of the major contributors to acid rain and urban smog which is a direct cause of serious diseases of respiratory and lung, hospitalization for heart, even premature death[3, 4] and destruction of the ozone layer[5]. In the absence of photocatalysts, NO is very stable and cannot be photolysed under visible light irradiation[6]. Semiconductor photocatalysis as an alternative to conventional approaches mediated advanced oxidation technology for degradation of environmental pollutants[7-10] is attracting the most attention, especially considering the characteristics of *in-situ* generating reactive radicals species (e.g. $^{\bullet}OH$) as strong oxidants, and the operating cost for the process can be reduced dramatically when solar energy is used[11, 12].

An ideal photocatalyst for practical use should be abundant, non-toxic, efficient and stable. As so far, various types of photocatalysts such as metal oxides, sulfides, nitrides or metal-free compounds etc. are developed to enhance photocatalytic performance[13-15]. Graphitic carbon nitrides (g-C_3N_4, noted as "CN") has been reported to be an efficient metal-free, low-cost photocatalyst and eco-friendly for air purification[16]. Pure CN is able to the removal of NO_x with low efficiency under visible light irradiation[1, 3] due to fast recombination rate of photogenerated electron–hole pairs[17]. In order to improve the photocatalytic performance of CN, different engineering strategies[18, 19] have been attempted such as microstructure engineering[20], tuning defects[21-23], constructing heterojunctions with metals[24], semiconductors[25].

Lowering the valence band of CN is required for producing more oxidizing electron holes for the advanced oxidation of pollutant using the hydroxyl radicals produced from the oxidizing holes from the valence bands. For instance, molecular engineering approaches such as potassium doping, carbon, and iron co-doping, incorporating electron-deficient pyromellitic dianhydride (PMDA) into the network of CN have been attempted to downwards shift the valence band of CN[26-28]. The addition of carbon dots can change the electronic band structure in terms of an enhanced light absorption, tune redox potential of the band structure and improve photoexcited

charge transfer[29]. Carbon dots modified CN binary or ternary photocatalysts have been prepared by different approaches for photocatalytic H_2 production and pollutants degradation recently[30-35]. In most cases, the carbon dots particles were deposited on bulk CN to construct interlayer heterojunction. The carbon dots worked as electron sinks that can facilitate interfacial electron transfer from bulk CN to the carbon dots sites and mediate further catalytic reaction. In addition, the hybrid photocatalysts exhibit stronger visible light absorption capability and enhanced photocatalytic performance partially due to the up-conversion photoluminescence property of carbon dots. In contrast, two-dimensional CN-based in-plane/intralayer heterostructure with carbon rings was developed for increasing separate the photoexcited electron-hole pair and accelerates the surface reaction kinetics for enhanced photoexcited carrier utilization[29]. This unique in-plane heterostructural carbon ring-CN nanosheet can expedite electron−hole pair separation and promote photoelectron transport through the local in-plane π-conjugated electric field, synergistically extending the photo carrier diffusion length and lifetime by 10 times relative to those achieved with pristine CN. Thus, tuning the location and junction condition of carbon dots with CN can alter the charge transfer property as well as electronic band structures of the hybrid photocatalyst, and a deep understanding of carbon dots modification effect on CN from molecular level is necessary.

In this study, we proposed a facile method to introduce graphitic carbon units in the CN matrix by the co-polymerization at a high temperature between m-phenylenediamine (MPD) and melamine in ambient air. We found that the addition of carbon-rich MPD does not increase the C/N ratio and total C+N content of the final polymer until a considerable carbon is precipitated. However, employing a small amount of MPD in the precursor, the graphitic carbon units were found to be in direct junction with the CN lattice forming an epitaxial junction. The specific in-plane junction assists the efficient transport of photoexcited charge carrier and creates the internal electric field that could modify the energy structure on the edge of the photocatalysts. Encouragingly, the band edge positions of as-prepared hybrid CN were downwards shifted up to about 1.0 V compared to pure CN via merging electron density of states of CN with that of graphitic carbon. The more positive valence band position of hybrid CN facilitates the production of $^{\bullet}OH$ for an efficient oxidation reaction and the amount of carbon species in the junction can be tuned

handily via the amount of MPD without additional effort. Moreover, these carbon-unit modified CN was, to our best knowledge, for the first time were used for the NO removal and the intermediate hydroxyl groups were observed directly form the in situ *in situ* diffuse reflectance infrared Fourier transform spectroscopy (DRIFTS).

Experimental

Photocatalysts were synthesized by the thermal treatment the mixture of melamine and MPD. In a typical run, MPD powder (0.02g) was dissolved in 2mL of ethanol solution, and then 2 g of melamine powders was added into the solution for a concentration of 1wt. % copolymerization. The mixture was stirred for two hours in a beaker, dried at 50 ^{o}C for 20 minutes to allow the evaporation of ethanol, transported into a crucible with a cover and then heated in a muffle furnace at a rate of 2.3 ^{o}C/min and kept for 4 h at 550 ^{o}C in ambient air. Similar treatments were performed for the different MPD levels by changing the concentration of MPD in ethanol. The thus prepared samples are denoted as CN-x (x is the weight percentage of the MPD in the mixture with melamine) and, e.g., the CN prepared using melamine with 1 wt. % MPD is noted as CN-1.

The X-ray diffraction (XRD) patterns of the prepared samples were determined at 2θ angles of 5.0–80^{o} (36 kV and 20 mA) on an XD-3 diffractometer (Persee, China) using monochromaticCu K_{α} radiation (λ = 1.54178 Å).^{13}C, ^{15}Nisotopeanalysis were carried out on an elemental analyzer-isotope ratio mass spectrometry(EA-IRMS, Pyro Cube-Isoprime 100, Elementar, UK) while the total C, H, O, and N content was measured on an elemental analyzer for organic materials (ElementarVario Micro Select, ElementarAnalysensysteme, Germany).UV-vis diffuse reflection spectra were characterized for all samples using a spectrophotometer equipped with an integrating sphere of 80 mm in diameter (UV-1800, MACY, China).Photoluminescence spectroscopy (PL) of the solid samples was obtained on FLS980 spectrofluorometer (Edinburgh Instrument, UK) with a 360 nm excitation wavelength. Thermal stability of the reactant and polymer products were carried out using the thermogravimetricanalysis (TGA) on a NETSCHZ F3 thermogravimeter (Germany) from room temperature to 800^{o}C under flowing N_2. Scanning electronic microscopy(SEM) of the as-prepared samples were examined on a field emission microscope (JSM7500F, JEOL, Japan). The transmission electron microscopy (TEM) images were

obtained from JEM2100 JEOL at an accelerating voltage of 200 keV. X-ray photoelectron spectroscopy (XPS) data were obtained on a ESCALAB.250Xi spectrometer (Thermofischer Scientific, USA) using monochromatic Al Kα X-rays (1486 eV) for the overall survey and high-resolution core level of C 1s. N 1s and O 1s. Fourier transformation infrared spectroscopy (FTIR) were recorded on a Nicolet iS5 (Thermo Fisher Scientific) spectrometer with an ancilliary sample holder for attenuated total reflectance Raman spectroscopy of the powders was recorded on an instrument from Horiba Scientific using a laser of 325 nm.

The photocatalytic activities of the as-prepared samples were evaluated by the degradation of Rhodamine B (RhB, 99 .5 % Macklin, China). The photocatalytic reaction was performed in a Pyrex reactor, where 0.1g catalyst of was dispersed in100mL RhB aqueous solution (8 μM in concentration). The photochemical reactor was illuminated using a 250 W xenon lamp with a cutoff filter to block the light under 400 nm or longer than 800 nm and the effective luminous intensity around 1 mW/cm^2.Flowing water was used to maintain the temperature of the reactor to be around 20 ^{o}C. During the irradiation, 5 mL of the suspension was taken out and centrifuged (5000 rpm, 5 min) to remove the photocatalysis before the light absorption measurement at 552 nm. In order to monitor the production of hydroxyl radicals, 20 mg of the CN or CN-x was suspended in 80 mL of an aqueous solutionof10mM NaOH and 3 mM p-phthalic acid. Thesuspension was stirred in the dark for 20 min to reach adsorption saturation before exposure to light's irradiation.4mL of the solution was collected from thereaction solution every 20 min and centrifuged to remove the solid photocatalyst. Photoluminescence spectroscopy at 320nm excitation was employed to determine the concentration of the 2-hydroxy p-phthalic acid.

Photocurrent measurements were performed on an electrochemical analyzer (Zennium Pro, Zahner, Germany) in a conventional three electrodes configuration with a gold mesh as the counter electrode, and Ag/AgCl as a reference electrode. Na_2SO_4 (0.5M) aqueous solution was used as the electrolyte. The working electrodes (1.0 cm^2) were prepared by spreading a slurry form 15 mg of samples, 10 μl of PEDOT and 50μl of water on FTO glass with glass rod using adhesive tapes as spacers[36].After drying in ambient air, the photoelectrodes were dried at 150 ^{o}C for 10 min.

The photocatalytic efficiency of bare CN, CN-1 and CN-5 under the visible-light irradiation (λ ≥

420 nm, 0.16 W cm^{-2}) was tested in a continuous photocatalytic reactor for NO removal[41]. A parent gas containing 100 ppm NO balance with He was first diluted to 550 ppb and then the NO flow (24 mL min^{-1}, 50% relative humidity) was then mixed with an air flow (2.4 L min^{-1}) before being introduced to the reaction reactor containing photocatalyst. The NO concentration of the effluent was continuously measured using a NO_x analyzer (Thermo Model 42i-TL). Also, the *in situ* diffuse reflectance infrared Fourier transform spectroscopy (DRIFTS) was recorded for the adsorption stage under the dark and photocatalytic process under visible-light illumination (AXe lamp, MVL-210, Japan) to determine the intermediate species [41].

Optimization of all geometric structures is carried out within the framework of the density functional theory (DFT) by means of the Cambridge Serial Total Energy Package[37] with a plane-wave basis set. The Perdew-Burke-Ernzernhof generalized gradient approximation is selected as the exchange-correlation function (ECF). The plane-wave cutoff energy is set to 400 eV and a 5×1×5 mesh was used. All the atomic positions are relaxed totally until the energy variation is less than 10^{-5}eV.Aftertheoptimization, the band structures, the density of states (DoS), and real space charge density maps of both systems were obtained by using the Nono Academic Device Calculator (Nanodcal) software package [38], which adopts the DFT combined the Keldyshnon equilibrium Green's function formalism (NEGF)[39]. During this computation, the local density approximation (LDA) [40] describes the ECF, and the valence electronic orbital's are expanded in a double-ς plus polarization (DZP) basis set for all atoms. The cutoff energy for the real space grid is set to 80 Hartree and 20×1×20 k-points mesh is employed in the Brillouin zone. For the calculated band structures, 500 k-points have been used and for calculating the DoS, 50×1×50 k-points mesh is selected.

Result and discussions

Different structures could exist in CN and a melon structure containing with inherent terminal amine groups and/or bridging secondary amine group is stable at 550 ^{o}C[42, 43]. After the isothermal calcination at 550 ^{o}C, the residual materials showed similar XRD patterns (Figure 1(a)) where only two obvious peaks were observed, indicating that addition of MPD does not change at large the layered structure of C_3N_4. The high-intensity peak at 27.40^{o}, corresponding to an interlayer distance of 0.326 nm, reflected the interlayer stacking of aromatic segments and can

be indexed as the (002) peak for the graphitic materials. However, a detailed analysis of the main peak showed a gradual shift to the higher angle. With a MPD level over the critical value of 3.5 %, the d-spacing for the (002) crystal planes (Figure 1(b)) keeps fairly stable at 0.327 nm. Generally, the shift of angle is related to the repulsion force between the graphitic layers depending on the atom content in the structure and thus there could be change in the C/N ration in the crystal lattice if the MPD level is lower than 3.5% rather than a composite of graphitic species and CN.

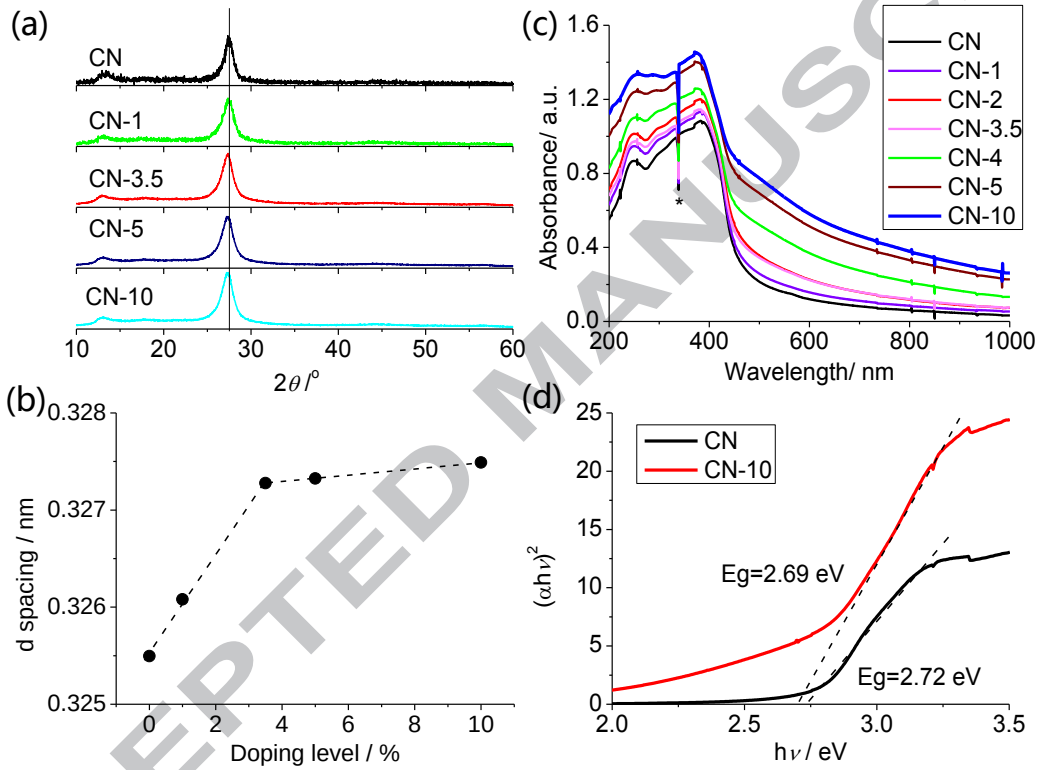

Figure 1. (a) XRD patterns for CN and MPD modified samples; (c) The corresponding d-spacings of the (002) crystal plane calculated from XRD; (c) UV-vis spectroscopy of the samples for the absorbance; (d) Tauc plots of the bare CN and CN-10 for the calculation of band gaps. The "*" mark in (c) indicates the peak induced by the change of light source in the spectrometer.

Compared to melamine, MPD doesn't contain nitrogen atom in the ring structure, but it contains the amine group for the polymerization process, which could affect the structure and the optical absorbance of the product. Figure 1(c) showed the light absorption of the MPD modified samples and it can be seen that the addition of MPD leads to an increase in the ultraviolet-visible (UV-vis) light absorption over the entire wavelength range between 200 and

1000 nm. The optical band gap, E_g, of a semiconductor can be estimated from the Tauc plots (Figure 1(d)), where the curve of converted $(\alpha h\nu)^2$ are plotted versus $h\nu$ from the UV-vis spectrum, in which α, h, and ν are the absorption coefficient, Planck constant, and light frequency, respectively[44]. A good linear region was found if m is equal 2 for a direct band gap. The CN-10 showed a slightly decreased E_g of 2.69 eV than CN, 2.72 eV by measuring the intercept between the linear region of the plot with the x-axis. For the samples with intermediate MPD levels, the change of E_g was even smaller, but the presence of an enlarged absorption tail could assist the light absorption and photocatalysis efficiency. In a previous study on the stoichiometry of CN[45, 46], the introduction of carbon vacancies expanded the band while the formation of nitrogen vacancies did the reverse. The slight change of band gap during the MPD modification may not change dramatically the composition of CN. The non-covalent doping of graphitic carbon in CN was not believed to change the edge of light absorption, but increases the absorption background extending to the near-infrared region,[36, 47] while the formation of nitrogen vacancies were reported to shorten the band gap of the C_3N_4: after the calcination in reducing atmosphere, a similar absorption curve was observed[46]. The gradual increase of absorbance in the UV-vis region indicates that there could be change in the matrix C_3N_4 structure while the increased absorption at 1000 nm could be related to the formation of graphitic carbon unit or the incorporation of benzyl units in the tri-s-triazine units. An abrupt increase of the absorption at 1000 nm was found if the MPD level increases from 3.5 % to 5 % (Figure S1), indicating that carbon-related species starts to accumulate significantly if the CN matrix was not able to tolerate the compositional change that might have caused by the addition of MPD. The present photocatalyst structure here is different from common carbon dots doped g-C_3N_4, since carbon dots were generally prepared beforehand and added to the precursors for C_3N_4[34, 35, 48], but in our work MPD with a benzyl ring and amine groups were added as the precursor. The deamonniation process during the condensation of precursors would induce the covalent boding between the carbon unit and triazine ring, and the redox potential of hybrid photocatalyst can be greatly modified by these junctions. Photoluminescence (PL) of the powders (Figure S2) showed a peak at 470 nm and did not change with the MPD modification, and a binding energy of excitons was calculated to be 0.1 eV for the for samples by comparing the photon energy for the band gap and emission peak. The decrease in PL intensity for the MPD-modified sample could be related to

the increased trapping center that decreased the radiative recombination of photoexcited charge carriers or the increased charge carrier transport that decreases the concentration of local electrons and holes[49].

The reaction between MPD and melamine is able to change the microstructure and composition of the final product and thus isotope C/N measurement was performed, and the detailed results were shown in Table 1. The C/N ratio (0.656) of melon ($C_{2.88}N_{4.32}H_{1.44}$) is coherent with those measured for the material synthesized from pure melamine in this study (0.665). The C/N ratio does not increase until the MPD content is higher than 5 %. For the δ values of the isotopic ^{13}C and ^{15}N increase constantly, indicating that part of the carbon or nitrogen in the product is ascribed to MPD during the deammonation process or the incorporation of benzyl ring into the s-triazine matrix since MPD showed low boiling point [50] of 284 ^{o}C and no product will be left behind at 550 ^{o}C in air. The thermal stability of melamine and MPD was investigated using TGA curve (Figure S3) and the differentiated TGA (dTG) peaked at 311 ^{o}C and 187 ^{o}C under flowing argon. The sample CN-3.5 showed the highest oxygen level (Table 1), which could be ascribed to the charge imbalance caused by the doping in the crystal structure and is consistent with the XPS spectroscopy (Figure S4), where a C=O or C-OH group can be verified after analyzing the binding energy of O1s and C1s. The temperatures for dTG peak can be correlated well to total oxygen content in the material if the MPD content is lower than 5 %: i.e. the increasing of oxygen content causes the decrease of peak temperature for dTG of the material in pure nitrogen gas, as shown in the TGA curves (Figure S5) as oxygen content in the structure of graphitic material is reported to destabilize the structure and induce a low-temperature ignition of the material[52]. It should be noted that there is a gradual weight loss above 700 ^{o}C for the CN-5 and CN-10 sample which could be related to the decomposition of graphite-related phases. The emergence of graphite indicates that the effect of MPD has been diverged to the production of a composite rather than the change of lattice which is in accord with the change of d-spacings with MPD level higher than 3.5 %. The raman spectroscopy (Figure S6(a)) of the CN, CN-1, CN-3.5 and CN-10 under UV light excitation showed similar peaks at at 1620, 1534, 1443, 1226, 978, 721, 571 and 483 cm^{-1}, corresponding to a melon structure[46]. No obvious Raman peaks for Carbon was generated and this could be related to the weak signals from them or the similarity in structure between triazine ring and carbon units. According to the FTIR spectra of the samples (Figure S6(b,

c)), the broader and less resolved peak for the breathing mode of the triazene group at 806-808 nm indicates lower structure order of the CN matrix as the incorporation of C from the MPD could be in the form of graphitic units or benzyl ring that induces defect to the melon structure[51]. Actually, the incorporation of C-unit into the triazine ring is a hole doping process and this is consistent with blue shift of breathing mode of the triazene group (Figure S6(c)) for those sample with MPD.

Table 1 Elemental analysis of the C_3N_4 samples with and without MPD modifications.

Sample	C at. %	N at. %	H at. %	O at. %	C/N at.	$\delta^{13}C$ ‰	$\delta^{15}N$ ‰
CN	46.418	30.430	21.592	1.560	0.656	-29.55	0.60
CN-1	45.896	30.138	23.291	2.129	0.657	-28.36	2.34
CN-3.5	45.002	29.480	22.947	3.427	0.655	-28.24	2.73
CN-5	45.461	30.188	22.601	2.515	0.664	-	-
CN-10	45.495	30.914	23.105	1.910	0.680	-27.52	3.58

SEM images (Figure S7) for CN and the representative CN-3.5 showed that both samples are composed of large plate-like structure on the scale of micrometer and fine particles around 20 nm. The detailed comparison showed that the larger and densely stacked plate like structures in CN were generally larger than CN-3.5. The size of the C_3N_4 sheet is also consistent with the TEM as shown in Figure 2 (a) and (e) and more importantly, CN showed scarce uniform dots of 4-10 nm in diameter on the surface while the CN-3.5 sample showed densely populated non-uniform dots with diameters less than 10 nm as shown in Figure 2(b) and (f), respectively. The structure of the dots on CN from melamine alone was found to contain tri-s-triazine group due to the higher extent of polymerizationthan melon during the calcination process in air. Tri-s-triazine base CN

can be synthesized in molten salt and it showed improved photocatalysis than the melon counterpart [53], but it is not fully stable thermodynamically from the polymerization in ambient air. A close-up image of adoton the CN-3.5 sample (Figure 2(f)) showed that it is composed of multiple regions with different interior domains. A detailed image analysis in Figure 2(g, h) indicates that it can be divided into the regions of graphitic carbon and tri-s-triazene. The incorporation of graphitic carbon unit in the adjacent areas of a triazine ring in the MPD modified C_3N_4 product from the mixed calcination of glucose and melamine is reported to accelerate the photoelectron transfer in the electrochemical system.[29] In this study, the intergrowth of the graphitic domain and tri-s-triazine domain is observed in small particles with an epitaxial growth between C_6N_7 and C_6 rings. The direct junction between the two components will cause the formation of dangling bounds or rings with imbalance charge, which can be resolved by the absorption of -OH, $-NH_2$ and *et al* on the surface or the boundary as in graphene oxide.[36] If the absorbed species reside in the intralayer structure could contribute partially to the increase of oxygen content in the structure upon modification with MPD, which is in accord with the elemental analysis.

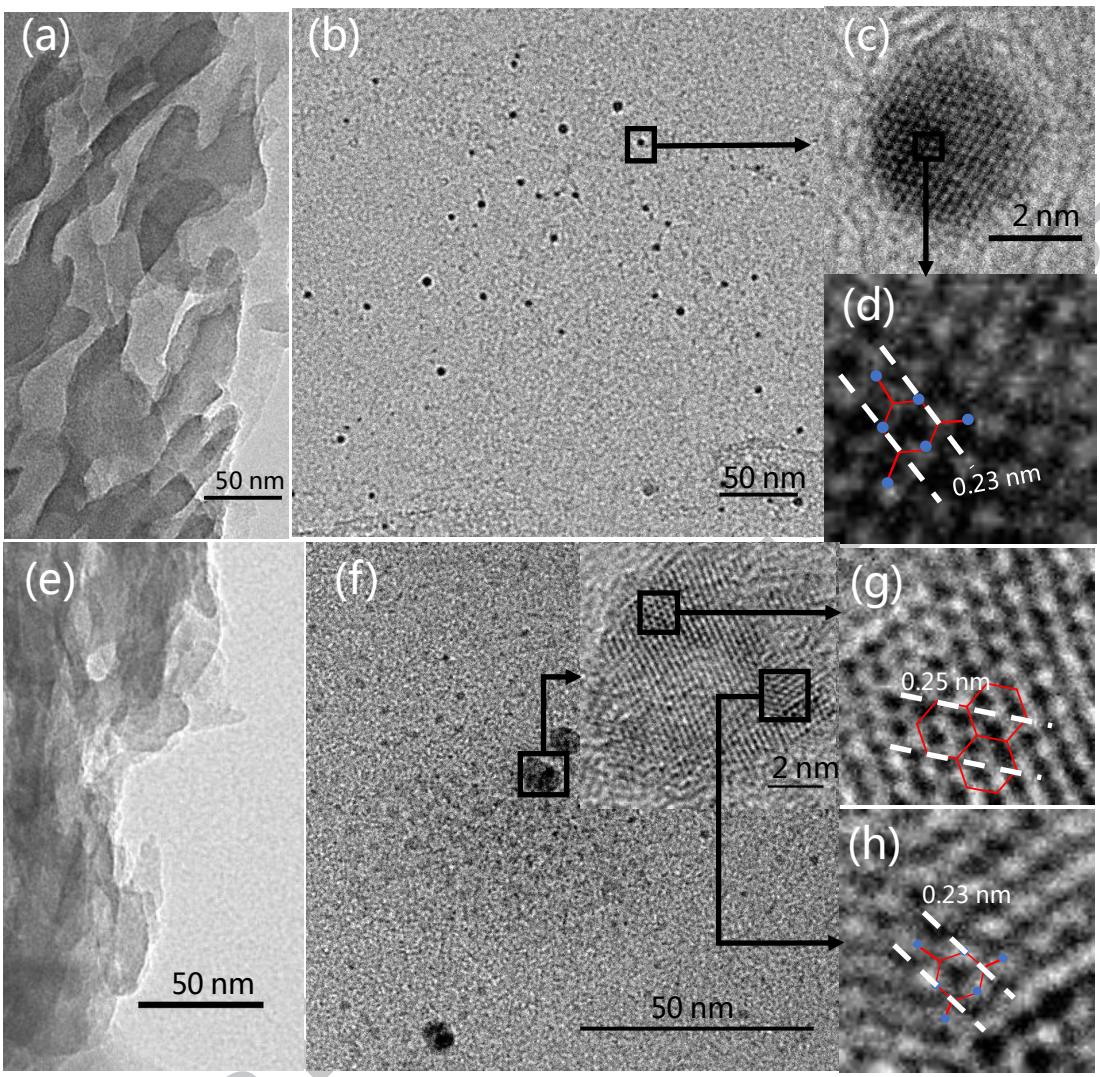

Figure 2. (a, b, c, d) TEM images of CN and (e, f, g, h) the CN-3.5. The drawing in (d) shows the structure of tri-s-triazine and the corresponding dspacing. The inset in (f) shows the enlarged image of the dot. The plane group and d spacing in (g) and (h) corresponds to that of graphite and tri-s-triazine, respectively.

In addition to the light absorption, the redox potential of band edges and charge-carrier dynamics, including the microscopic dynamic process of the charge generation, recombination, separation, and transfer, play crucial roles in determining the photocatalytic performance.[54] Especially, the energy position of band edges is crucially important for the photocatalytic efficiency as they determine the oxidizing and reduction capability of the hot holes from the valence band or electrons from the conduction band, respectively. We used Mott-Schottky to measure the flat band of the semiconductor in aqueous solution under the dark condition to estimate the energy level of band edges as for n- or p- semiconductors the band edge is close to

the flat band[55]. The Mott-Schottky plots of the samples were shown in Figure 3 (a), where the square of space charge capacitance, C^2, is plotted against bias on the semiconducting electrode. The space charge capacitance was calculated from the electrochemical impedance stereoscopy using the Brug's method to resolve the pseudo-capacitance.[56] The positive slope is indicative of n-type semiconductors for all the samples.[57]The flat band potential of g-C_3N_4 in neutral 0.1 M Na_2SO_4 solution is determined to be -1.10 V vs Ag/AgCl (or -0.90 vs NHE) by the intersection between extrapolation of the linear region and x-axis, which is slightly higher than the reported values -1.13 V vs NHE under similar conditions.[58] Remarkably, the flat band of the CN-1 showed a dramatic change and the chemical redox potential increased to -0.16 V vs Ag/AgCl. For CN as an n-type semiconductor, the conduction band potential is more negative by about −0.2 V than the flat-band potential[54, 59], and thus the redox potential of conduction band for CN-1 is estimated to be -0.36 V vs Ag/AgCl (-0.16 V vs NHE), which is similar to the value from ultraviolet photoemission spectroscopy for carbon dots doped C_3N_4.[60] As the working function of graphene is calculated to be 4.66 eV and the flat band and conduction band of the CN-1 is calculated to be -4.42 eV and -4.62 eV versus the energy of vacuum, respectively. These results indicate that the charge transfer between the fine graphitic carbon and CN would lower the energy level of the material[29]. However, with the increase of MPD above 1 %, the redox potential decreased gradually comparing to CN-1. A decrease of redox potential of CN has been observed in the incorporation of graphene oxide[36] as large graphitic carbon (8-10 nm in diameter) starts to show for CN-3.5. The elemental analysis indicates the decrease of total C+N in the matrix, which can be related to the oxygenation of the polymer, as evidence by the XPS results (detailed spectra and analysis in Figure S4).

The currents at different potentials induced by the photoexcited charge carriers are also performed under the same condition of Mott-Schottky measurements.[57, 61] The steady-state photocurrent measured at 0.5 V vs Ag/AgCl (Figure3(c)) showed that the photoelectrode with CN-1 presented a larger anodic photocurrent than the one with CN, while the one with CN-10 presented a lower photocurrent than pure CN. Notably, the photocurrent at 0.5 V vs Ag/AgCl for CN-1 at 0.5 V, 6 $\mu A\ cm^{-2}$, is 1.6 times higher than CN, 2.3 $\mu A\ cm^{-2}$. The modification with MPD improved the photocurrent stability during the electrochemical testing: i.e. CN showed a gradual

decrease of photocurrent during the 60 seconds under illumination while the MPD-modified samples are stable in the 60 seconds with lights on. The decrease of photocurrent for the CN sample under illumination could be related to the oxidation process of the electrode due to the charge carrier transport limitations.[62] For the photovoltammograms of CN and CN-x under chopped visible light (wavelength >400 nm) were recorded in Figure 3(d), where the MPD-modified samples show enhanced cathodic and anodic photocurrent than CN if MPD level is lower than 3.5 %. In a previous report, oxygen doping in CN was reported to increase the hydrogen evolution reaction as well as the oxygen evolution reaction, but the oxygen doping in carbon-nitride aerogel seems to decrease the redox potential of the conduction band and the bandgap, E_g[63]. As we observed a significant increase in the redox potential of conduction band, the effect of oxygen in our case should be minor.

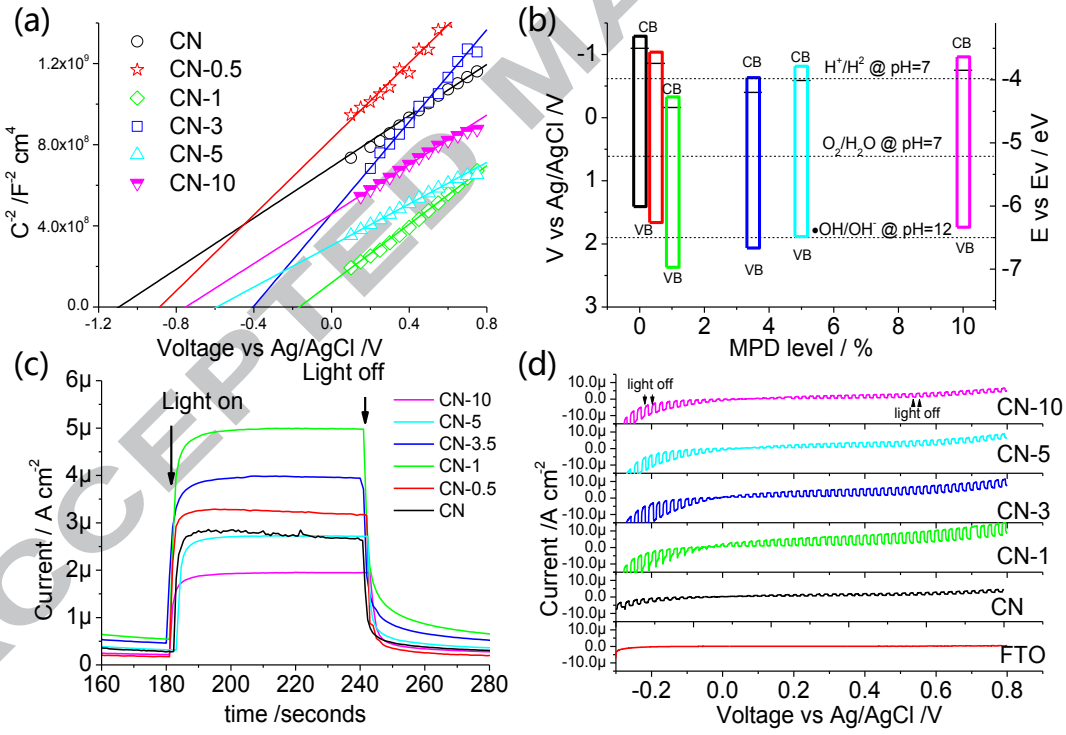

Figure 3. (a)Mott-Schottky plots of the representative samples and (b) the corresponding band structure, where the correlation between the redox potential and the energy level in referred to vacuum energy is presented; (c) Steady-state chronoamperometry at 0.5 V versus Ag/AgCl reference under dark and illuminated condition; (d) photovoltammograms of the samples and the bare FTO.

For an in-depth understanding of the relationship between the in-plane heterostructure and photocatalytic activity, the first-principle calculations of energy and band structure were performed. As most of the polymorphs of CN were calculated to be a semiconducting character,[29, 64] while graphitic carbon is showed to be metallic due to the in-plane π boding but insulating in a direction at a right angle to the plane. As melamine is slightly soluble in ethanol while MPD is soluble, the admixture before the calcination is actually a core-shell structure and the deammonation and graphitization is possible on the surface. The junction between the graphitic layer the tri-s-triazine layer can be in the form of intralayer covalent bond and non-covalent interlayer bonding. In the former, the real space charge density maps Figure 4(a)showed that the tertiary carbon either inside the tri-s-triazine structure or on the interface for the junction showed higher density of electron cloud. Under either way of junction, there is in-gap density of state and bands crossing the Fermi level (Figure 4 (c, d) and Figure S8): the one with non-covalent bonding showed continuous density of state (DoS) while the one with intralayer junction showed scattered DoS near the Fermi level. The discontinuous energy gap explains the expanded light absorption in the intra-layer junction, which is unlike the increase of absorption background in the non-covalent junction as reported in multiple reports[36, 47]. As reported in the metallic photocatalyst, the electrons on the Fermi level could reduce the electric field for the separation of photoexcited charge carriers[65], but if these domain is on the scale of nanometer as in this study, it will increase the kinetics of charge transport while preserving the high electric field[66]. The metallization of a semiconductor via surface coating is reported to cause the internal space-charged region in the metal and semiconductor surface and, in extreme case, the Fermi level of this Shockley junction will be in a small range, which is termed as “Fermi level pinning”.[67] Because graphite/graphene is a semimetal with free in-plane electron, the covalent bonding between the tri-s-triazine ring can form such junction and interfacial space-charged region. From this point of view, it would not be surprised that the flat band of the sample with MPD decreased to match the work function of graphene at low MPD level since the charge transport through the covalent bonding is fast to maintain the thermal equilibriumbetween the graphitic region and tri-s-triazine region and the electric field in the confined region is strong enough to maintain the space-charged region. With higher MPD level than 1.0 %, the possible increase of the domain area of graphitic subunit will decrease the

electric field across the carbon/CN interface to maintain the Fermi level pinning and thus an increase of band edges are observed. Moreover, with the precipitate of independent graphitic fragment at higher MPD level, the redox potential of the flatband is reported to increase with the non-covalent graphene content[36]

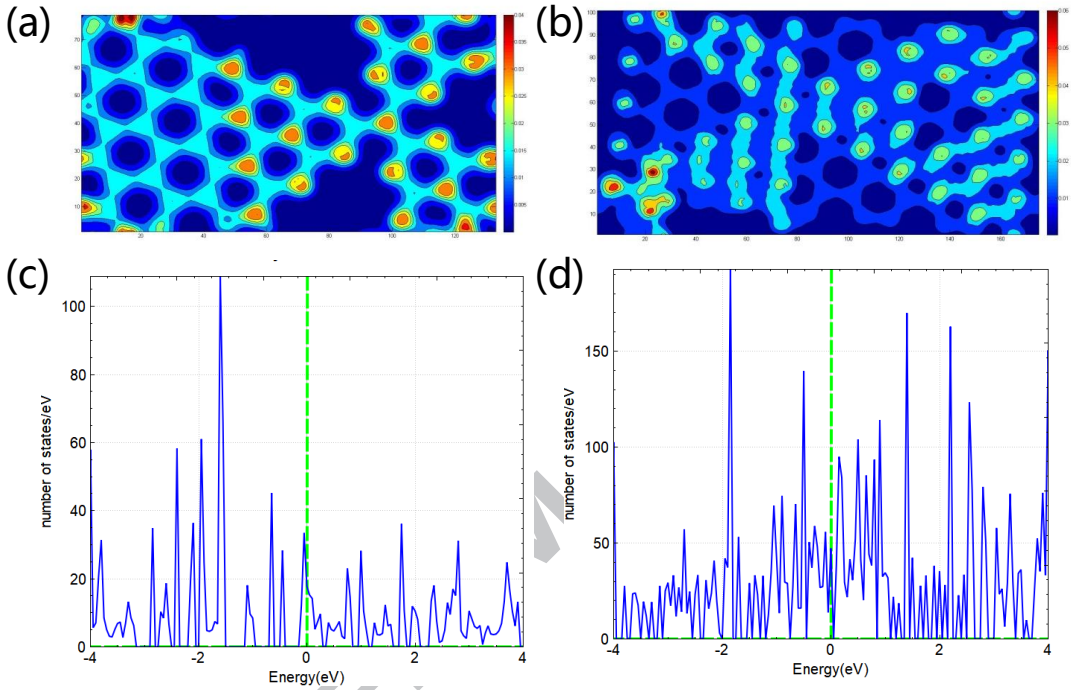

Figure 4. Real-space charge density maps and the DoS diagrams for the intralayer (a, c) and interlayer (b, d) junction between graphitic and tri-s-triazine domain. The space charge density of graphitic carbon is at the bottom layer of the image (b).

The increase of chemical redox potential indicating the lowering of flat band and enhance the oxidizing ability of the hot holes produced in the valence band. It is known that terephthalic acid (TA) can be oxidized by $^{\bullet}$OH radicals to produce 2-hydroxyterephthalic acid (TAOH), emitting a unique photoluminescence (PL) signal at 426 nm.[58] The clear observation of gradually increased PL emission peaks (Figure 5) after the elongated light irradiation could prove the formation of $^{\bullet}$OH radicals during the light illumination. The CN-1 increased the productivity by 1.35 times in the 100 minutes' duration than CN though they show quite similar absorption curve and E_g. Although CN-3.5 showed a larger light absorption, it showed slightly inferior performance in the TAOH production than CN-1 due to the higher redox potential of the valence band. The production of hydroxyl radicals can be achieved via (1) the combination of hot electrons from the

conduction band to the absorbed oxygen species to from reactive oxygen species as intermediates or (2) the combination of electron holes with water[68]. The lowering of valence band would increase the oxidation ability of the hot holes from our study and boosting the production of hydroxyl radicals from the second routes. The CN-10 sample showed 80 % productivity of CN after 100 minutes' illumination, which can be ascribed to the increased graphitic center that caused the recombination of photoexcited hole-electron pair. Figure S(9) showed that the dye degradation was also performed to evaluate the oxidizing ability of the carbon nitrides. CN-3.5 showed the best performance under a xenon lamp equipped with a filter to block the light under 400 nm in wavelength. Compared with the CN from melamine, it accelerated the degradation rate of RhB by a factor of 2 under visible light >400 nm. With higher MPD level than 3.5 %, the degradation kinetics is no better than CN as a result of the increased recombination sites caused by the overloading of graphite-related species. Comparing to the experiment on TA oxidation, the distinct color of RhB would affect the absorption and the charge transfer between the dye and photocatalyst would also contribute to the decoloration process[69].

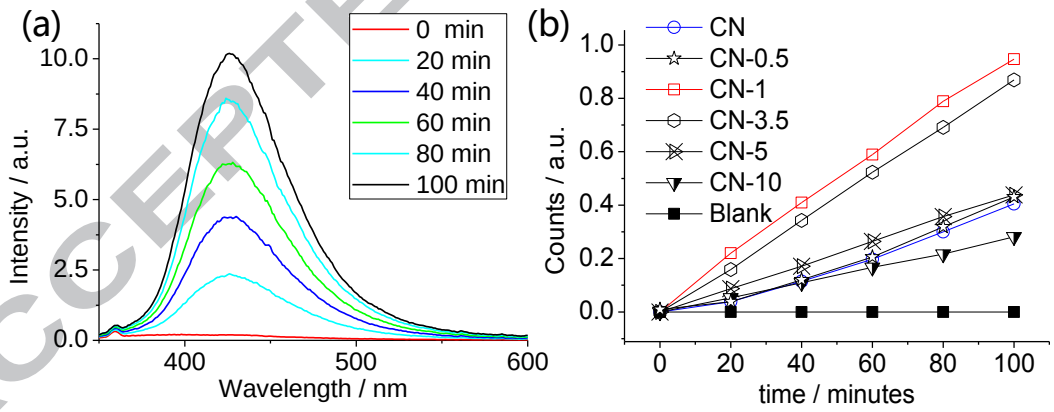

Figure 5. (a) PL spectrum of 2-hydroxyterephthalic acid generated by reacting terephthalic acid with $^{\bullet}OH$ radicals in an aqueous suspension of the CN-1; (b)time-dependent fluorescence signal intensity at 426 nm for CN and CN-x samples. The blank experiment is performed without photocatalyst.

The photocatalytic efficiency of bare CN and CN-1 and CN-5 were tested under the visible-light irradiation (λ ≥ 420 nm) in continuous photocatalytic reactor for NO removal. The visible light was

switched on after reaching the adsorption equilibrium. Figure (6) shows the variation of NO concentration over the as-prepared samples (C/C^0 x 100%) with irradiation time. The maximum NO purification ratio got after nearly 6 minute for all samples due to the photocatalytic reaction. The NO removal ratio reach stable for all samples and the NO removal ratio after 30 minutes were obtained 23.4%, 34% and 15% for CN, CN-1 and CN-5, respectively, while the final NO concentration for the reaction with CN-0.5 and CN-3.5 is quite similar to CN. The NO removal ratio for the best CN-1 sample is actually much better than the other compositions and CN reported in the reference [45]. Even though other modified samples showed higher UV-vis light absorbance, but their valence band positions determined that generation of hydroxyl radicals could not be efficient as that of CN-1 as shown in Fig. 5b.

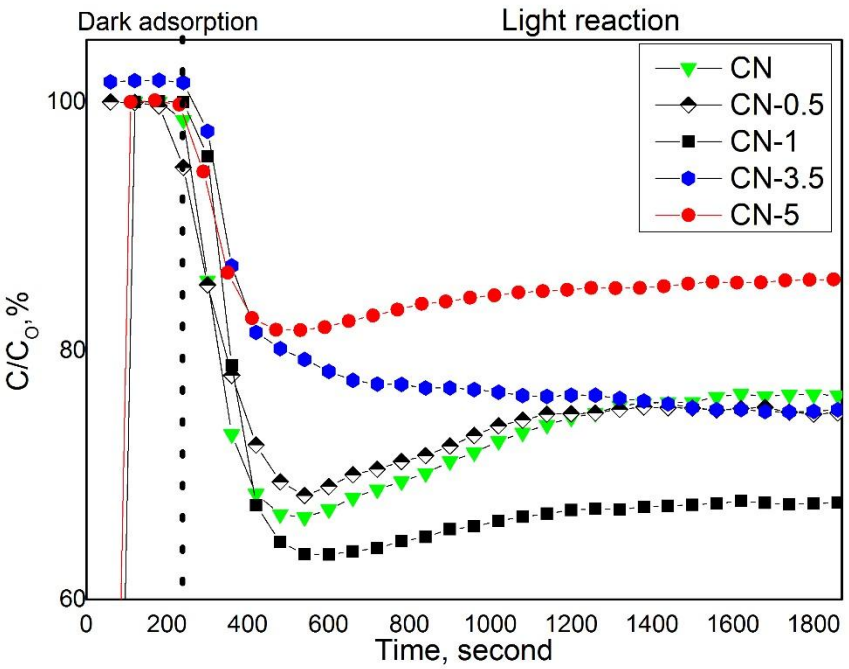

Figure 6. Photocatalytic efficiency toward NO removal under visible light irradation (λ>400 nm)

In order to demonstrate the effect of MPD-modifications on the intermediate products, in situ DRIFTS were performed on the sample under NO. The adsorption evolution of NO on CN-1 showed much stronger signal than the pristine one in terms of intermediate products as shown from the signal of the in-situ DRIFTS in Figure 7. The peaks at 1102 and 1049 cm^{-1} corresponding to adsorption $NO_2^-$and NO_3^-, respectively[6] are distinguishable when CN-1 is present. The

adsorption bands at 863 and 911 cm^{-1} assigned to chelated nitrite and N_2O_4 are also more intense for the MPD modified samples and both of them were increases with time. Most importantly, two peaks at 3452 and 3557 cm^{-1} (Figure 7 (d)) assigned to ν(OH) mode of isolated H_2O and ν(OH) of NO–H [2] present only when CN-1 is used as the photocatalyst. The evolution of ν(OH) bonds is linked to the energy level of the superficial layer of the catalyst and the downward shift of the flat band of CN-1 could induce stronger bonding between the hydroxyl group on the surface. Upon the introduction of oxygen species, CN donate the lone pair electron from its triazine N atom to O_2 to form the reactive oxygen species (ROS) following the route of O_2^- to H_2O_2 and then $^{\bullet}OH$ radicals[70]. These reaction species will combine with the NO to give the adsorbed intermediate products, such as NO_2^-, NO_3^- and etc. [71], but it seems that the signals from the pristine CN is much weaker in either the nitrogen-containing species or the $^{\bullet}OH$ radicals than the one with CN-1. In CN-1, the direct junction between the tri-s-triazine ring and graphitic unit will cause electron accumulation on the graphitic carbon atom[33] while leaving the pyridine carbon atom more positively charged than the one in a normal CN. The carbon on the interface can attract the lone pair electron from water and NO to produce the OH group in isolated H_2O and NO-H as evidenced by the in situ DRFTS.

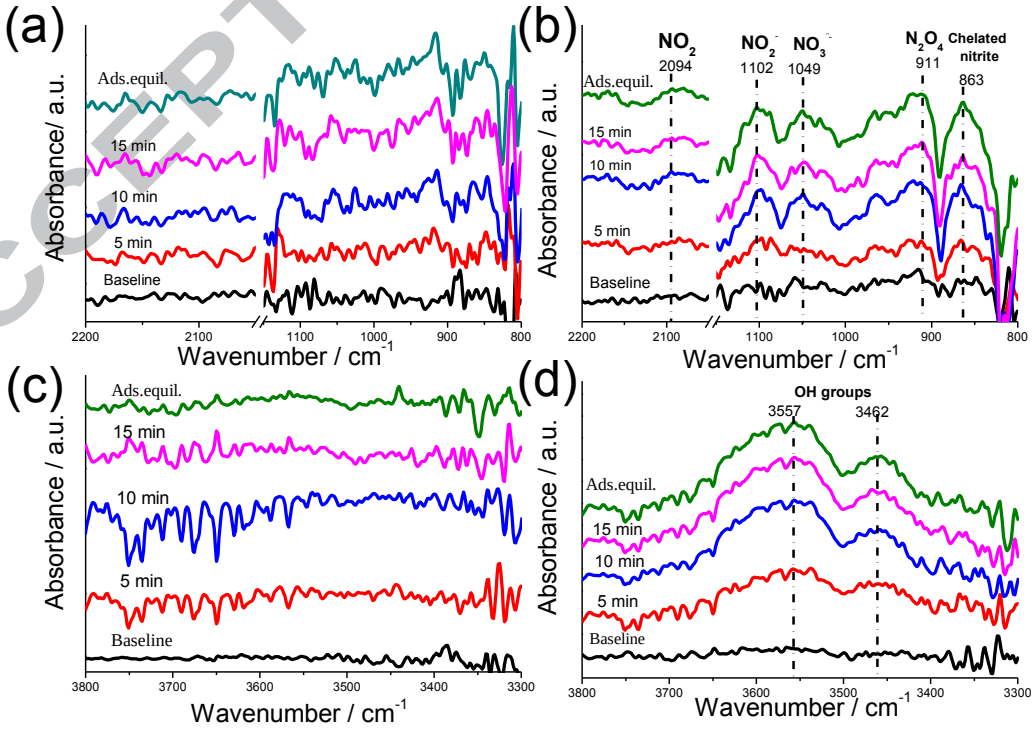

Figure 7. In situ DRIFTS spectra for the stage of NO adsorption under the dark for the CN (a, c) and CN-1 (b, d). (a, c) and (b, d) show the different range of wavenumber.

Figure 8 shows in situ DRIFTS of the photocatalytic reactions with the pure CN and CN-1. The reaction peaks for the NO_2 (2099-2094 cm^{-1}), NO_2^- (1111-1106 cm^{-1})[72]and NO_3^- (1047-1049 cm^{-1})[6] intermediates are quite similar in shape, but the absorbance are much higher and stronger for CN-1 than that for CN (Figure S10 (a-c)). As shown in Figure 8(a), the two absorption bands at 868 and 884 cm^{-1} are assigned to chelated nitrite and NO_2^-[41], corresponding to those at 866 and 881 cm^{-1} for CN-1 in (b). For the CN-1, the bands at 3462 and 3557 cm^{-1}, assigned to v(OH) mode of isolated H_2O and NO–H, respectively, decrease in intensity, and this can be explained by two facts: (1) these negatively charged OH groups adsorbed on MPD-modified material were replaced by of another negative fragment ($NO_2^-$and NO_3^-) and (2) they are consumed during the oxidation of the intermediate species [2, 71]. In contrast, the omission of the bands for the OH in the spectra for CN indicate that the contribution from the ROS are the dominant reactants in the oxidation process while the hydroxyl group would be also important to the oxidation process of NO in the case of CN-1.

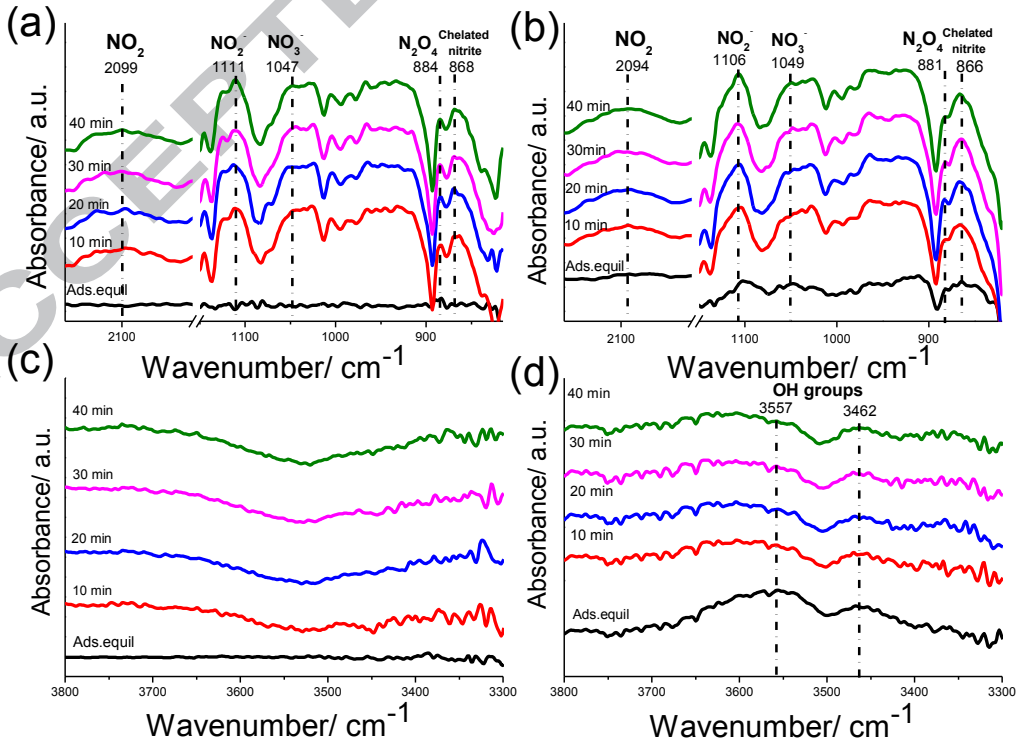

Figure 8. In situ DRIFTS spectra for the stage of NO adsorption under visible light for the CN (a, c) and CN-1 (b, d). (a, c) and (b, d) show the different range of wavenumber.

Conclusions

In summary, a facile method has been demonstrated to fabricate in-situ graphitic carbon units in CN matrix to improve the photo oxidation property of this metal-free catalyst. The graphitic carbon units evolved in-situ can tune the energy level of the band edges on the scale of 1.0 eV, which improves the versatility of the photocatalysts. The dramatic change of flatband with a small number of graphitic domains can be attributed to the internal electric field on the carbon/CN interface due to the fast charge carrier transport in the confined area. The addition MPD also improves the light absorption and photoelectron chemical stability of the parent material. The catalyst is around 1.35 time more efficient for CN-1 than CN in producing $^{\bullet}OH$ radicals for the photo-induced oxidation process possibly by changing the band edge energy. In NO purification model, the CN-1 improves the activity in NO oxidization under visible light by increasing the various intermediates and final species than CN. This could be related to the band edge position and its ability to adsorb nitrites and the hydroxyl group(OH) on material surface which transformed to different nitrates forms by photogenerated holes.

Acknowledgement

We would like to acknowledge the support fromthe Natural Science Foundation of China (NSFC, 51702264, 41371275，51708153), National Key Research and Development Program of China (grant No. 2018FYD0200701), the Fundamental Research Funds for the central universities (XDJK2017B033, XDJK2019D042) and Research Funding of Southwest University (SWU117019).

References

[1] J. Luo, G. Dong, Y. Zhu, Z. Yang, C. Wang, Switching of semiconducting behavior from n-type to p-type induced high photocatalytic NO removal activity in g-C_3N_4, Appl. Catal. B 214 (2017) 46-56.

[2] J.C.S. Wu, Y.-T. Cheng, In situ FTIR study of photocatalytic NO reaction on photocatalysts under UV irradiation, J. Catal. 237 (2006) 393-404.

[3] F. Dong, Z. Zhao, Y. Sun, Y. Zhang, S. Yan, Z. Wu, An Advanced Semimetal–Organic Bi Spheres–g-C3N4 Nanohybrid with SPR-Enhanced Visible-Light Photocatalytic Performance for NO

Purification, Environ. Sci. Technol. 49 (2015) 12432-12440.

[4] F. Dong, Z. Wang, Y. Li, W.-K. Ho, S.C. Lee, Immobilization of Polymeric g-C3N4 on Structured Ceramic Foam for Efficient Visible Light Photocatalytic Air Purification with Real Indoor Illumination, Environ. Sci. Technol. 48 (2014) 10345-10353.

[5] C. Su, X. Ran, J. Hu, C. Shao, Photocatalytic Process of Simultaneous Desulfurization and Denitrification of Flue Gas by TiO2–Polyacrylonitrile Nanofibers, Environ. Sci. Technol. 47 (2013) 11562-11568.

[6] Y. Zhou, Z. Zhao, F. Wang, K. Cao, D.E. Doronkin, F. Dong, J.-D. Grunwaldt, Facile synthesis of surface N-doped Bi2O2CO3: Origin of visible light photocatalytic activity and in situ DRIFTS studies, J. Hazard. Mater. 307 (2016) 163-172.

[7] B.M. da Costa Filho, A.L.P. Araujo, G.V. Silva, R.A.R. Boaventura, M.M. Dias, J.C.B. Lopes, V.J.P. Vilar, Intensification of heterogeneous TiO2 photocatalysis using an innovative micro-meso-structured-photoreactor for n-decane oxidation at gas phase, Chemical Engineering Journal 310 (2017) 331-341.

[8] M. Ou, F. Dong, W. Zhang, Z. Wu, Efficient visible light photocatalytic oxidation of NO in air with band-gap tailored $(BiO)_2CO_3$–BiOI solid solutions, Chem. Eng. J. (Lausanne) 255 (2014) 650-658.

[9] W.C. Huo, X.a. Dong, J.Y. Li, M. Liu, X.Y. Liu, Y.X. Zhang, F. Dong, Synthesis of Bi_2WO_6 with gradient oxygen vacancies for highly photocatalytic NO oxidation and mechanism study, Chem. Eng. J. (Lausanne) 361 (2019) 129-138.

[10] F. Dong, H. Liu, W.-K. Ho, M. Fu, Z. Wu, $(NH_4)_2CO_3$ mediated hydrothermal synthesis of N-doped (BiO)2CO3 hollow nanoplates microspheres as high-performance and durable visible light photocatalyst for air cleaning, Chem. Eng. J. (Lausanne) 214 (2013) 198-207.

[11] L.-S. Zhang, K.-H. Wong, H.-Y. Yip, C. Hu, J.C. Yu, C.-Y. Chan, P.-K. Wong, Effective Photocatalytic Disinfection of E. coli K-12 Using AgBr–Ag–Bi_2WO_6 Nanojunction System Irradiated by Visible Light: The Role of Diffusing Hydroxyl Radicals, Environ. Sci. Technol. 44 (2010) 1392-1398.

[12] G. Zhang, W. Choi, S.H. Kim, S.B. Hong, Selective photocatalytic degradation of aquatic pollutants by titania encapsulated into FAU-type zeolites, J. Hazard. Mater. 188 (2011) 198-205.

[13] J. Hui, G. Zhang, C. Ni, J.T.S. Irvine, Promoting photocatalytic H2 evolution by tuning cation deficiency in La and Cr co-doped SrTiO3, Chem. Commun. (Cambridge, U. K.) 53 (2017) 10038-10041.

[14] G. Zhang, G. Liu, L. Wang, J.T.S. Irvine, Inorganic perovskite photocatalysts for solar energy utilization, Chem. Soc. Rev. 45 (2016) 5951-5984.

[15] T. Giannakopoulou, I. Papailias, N. Todorova, N. Boukos, Y. Liu, J. Yu, C. Trapalis, Tailoring the energy band gap and edges' potentials of g-C3N4/TiO2 composite photocatalysts for NOx removal, Chem. Eng. J. (Lausanne) 310 (2017) 571-580.

[16] Z. Wang, Y. Huang, W. Ho, J. Cao, Z. Shen, S.C. Lee, Fabrication of Bi2O2CO3/g-C3N4 heterojunctions for efficiently photocatalytic NO in air removal: In-situ self-sacrificial synthesis, characterizations and mechanistic study, Appl. Catal. B 199 (2016) 123-133.

[17] X. Liu, J. Liang, X. Song, H. Yang, X. Li, H. Dai, Y. Song, Y. Liu, J. Hu, X. Pan, X. OuYang, Z. Liang, Enhanced water dissociation performance of graphitic-C3N4 assembled with ZnCr-layered double hydroxide, Chem. Eng. J. (Lausanne) 337 (2018) 560-566.

[18] X. Dong, F. Cheng, Recent development in exfoliated two-dimensional g-C_3N_4 nanosheets for photocatalytic applications, J. Mater. Chem. A 3 (2015) 23642-23652.

[19] Z. Lu, D. Liu, J. Zhou, F. Dong, Lower treating temperature leading to higher air purification activity, Chem. Eng. J. (Lausanne) 314 (2017) 640-649.

[20] H.W. Huang, K. Xiao, N. Tian, F. Dong, T.R. Zhang, X. Du, Y.H. Zhang, Template-free precursor-surface-etching route to porous, thin *g*-C_3N_4 nanosheets for enhancing photocatalytic reduction and oxidation activity, J. Mater. Chem. A 5 (2017) 17452-17463.

[21] W. Cui, J. Li, W. Cen, Y. Sun, S.C. Lee, F. Dong, Steering the interlayer energy barrier and charge flow via bioriented transportation channels in g-C_3N_4: Enhanced photocatalysis and reaction mechanism, J. Catal. 352 (2017) 351-360.

[22] T. Xiong, W. Cen, Y. Zhang, F. Dong, Bridging the g-C_3N_4 Interlayers for Enhanced Photocatalysis, ACS Catal. 6 (2016) 2462-2472.

[23] Y.H. Li, W.K. Ho, K.L. Lv, B.C. Zhu, S.C. Lee, Carbon vacancy-induced enhancement of the visible light-driven photocatalytic oxidation of NO over g-C3N4 nanosheets, Appl. Surf. Sci. 430 (2018) 380-389.

[24] G. Jiang, X. Li, M. Lan, T. Shen, X. Lv, F. Dong, S. Zhang, Monodisperse bismuth nanoparticles decorated graphitic carbon nitride: Enhanced visible-light-response photocatalytic NO removal and reaction pathway, Appl. Catal. B 205 (2017) 532-540.

[25] X.Z. Li, W. Zhu, X.W. Lu, S.X. Zuo, C. Yao, C.Y. Ni, Integrated nanostructures of CeO_2/attapulgite/g-C_3N_4 as efficient catalyst for photocatalytic desulfurization: Mechanism, kinetics and influencing factors, Chem. Eng. J. (Lausanne) 326 (2017) 87-98.

[26] Z. Shouwei, L. Jiaxing, Z. Meiyi, L. Jie, X. Jinzhang, W. Xiangke, Bandgap Engineering and Mechanism Study of Nonmetal and Metal Ion Codoped Carbon Nitride: C+Fe as an Example, Chem. Eur. J. 20 (2014) 9805-9812.

[27] M. Zhang, X. Bai, D. Liu, J. Wang, Y. Zhu, Enhanced catalytic activity of potassium-doped graphitic carbon nitride induced by lower valence position, Appl. Catal. B 164 (2015) 77-81.

[28] S. Chu, Y. Wang, Y. Guo, J. Feng, C. Wang, W. Luo, X. Fan, Z. Zou, Band Structure Engineering of Carbon Nitride: In Search of a Polymer Photocatalyst with High Photooxidation Property, ACS Catal. 3 (2013) 912-919.

[29] W. Che, W. Cheng, T. Yao, F. Tang, W. Liu, H. Su, Y. Huang, Q. Liu, J. Liu, F. Hu, Z. Pan, Z. Sun, S. Wei, Fast Photoelectron Transfer in (Cring)–C_3N_4 Plane Heterostructural Nanosheets for Overall Water Splitting, J. Am. Chem. Soc. 139 (2017) 3021-3026.

[30] K. Wang, X. Wang, H. Pan, Y. Liu, S. Xu, S. Cao, In situ fabrication of CDs/g-C_3N_4 hybrids with enhanced interface connection via calcination of the precursors for photocatalytic H_2 evolution, Int. J. Hydrogen Energy 43 (2018) 91-99.

[31] F. Wang, Y. Wang, Y. Feng, Y. Zeng, Z. Xie, Q. Zhang, Y. Su, P. Chen, Y. Liu, K. Yao, W. Lv, G. Liu, Novel ternary photocatalyst of single atom-dispersed silver and carbon quantum dots co-loaded with ultrathin g-C_3N_4 for broad spectrum photocatalytic degradation of naproxen, Appl. Catal. B 221 (2018) 510-520.

[32] Z. Xie, Y. Feng, F. Wang, D. Chen, Q. Zhang, Y. Zeng, W. Lv, G. Liu, Construction of carbon dots modified MoO_3/g-C_3N_4 Z-scheme photocatalyst with enhanced visible-light photocatalytic activity for the degradation of tetracycline, Appl. Catal. B 229 (2018) 96-104.

[33] F. Guo, W. Shi, W. Guan, H. Huang, Y. Liu, Carbon dots/g-C_3N_4/ZnO nanocomposite as efficient visible-light driven photocatalyst for tetracycline total degradation, Sep. Purif. Technol. 173 (2017) 295-303.

[34] S. Fang, Y. Xia, K. Lv, Q. Li, J. Sun, M. Li, Effect of carbon-dots modification on the structure and photocatalytic activity of g-C_3N_4, Appl. Catal. B 185 (2016) 225-232.

[35] H. Zhang, L. Zhao, F. Geng, L.-H. Guo, B. Wan, Y. Yang, Carbon dots decorated graphitic carbon

nitride as an efficient metal-free photocatalyst for phenol degradation, Appl. Catal. B 180 (2016) 656-662.

[36] Y. Zhang, T. Mori, L. Niu, J. Ye, Non-covalent doping of graphitic carbon nitride polymer with graphene: controlled electronic structure and enhanced optoelectronic conversion, Energy Environ. Sci. 4 (2011) 4517.

[37] M.D. Segall, J.D.L. Philip, M.J. Probert, C.J. Pickard, P.J. Hasnip, S.J. Clark, M.C. Payne, First-principles simulation: ideas, illustrations and the CASTEP code, J. Phys.: Condens. Matter 14 (2002) 2717.

[38] J. Taylor, H. Guo, J. Wang, Ab initio modeling of quantum transport properties of molecular electronic devices, Phys. Rev. B 63 (2001).

[39] B.G. Wang, J. Wang, H. Guo, Current partition: A nonequilibrium Green's function approach, Phys. Rev. Lett. 82 (1999) 398-401.

[40] I.V. Solovyev, P.H. Dederichs, V.I. Anisimov, CORRECTED ATOMIC LIMIT IN THE LOCAL-DENSITY APPROXIMATION AND THE ELECTRONIC-STRUCTURE OF D-IMPURITIES IN RB, Phys. Rev. B 50 (1994) 16861-16871.

[41] J. Li, Z. Zhang, W. Cui, H. Wang, W. Cen, G. Johnson, G. Jiang, S. Zhang, F. Dong, The Spatially Oriented Charge Flow and Photocatalysis Mechanism on Internal van der Waals Heterostructures Enhanced *g*-C_3N_4, ACS Catal. 8 (2018) 8376-8385.

[42] G.G. Zhang, Z.A. Lan, X.C. Wang, Conjugated Polymers: Catalysts for Photocatalytic Hydrogen Evolution, Angew. Chem. Int. Ed. 55 (2016) 15712-15727.

[43] F. Fina, S.K. Callear, G.M. Carins, J.T.S. Irvine, Structural Investigation of Graphitic Carbon Nitride via XRD and Neutron Diffraction, Chem. Mater. 27 (2015) 2612-2618.

[44] C. Ni, G. Hedley, J. Payne, V. Svrcek, C. McDonald, L.K. Jagadamma, P. Edwards, R. Martin, G. Jain, D. Carolan, D. Mariotti, P. Maguire, I. Samuel, J. Irvine, Charge carrier localised in zero-dimensional $(CH_3NH_3)_3Bi_2I_9$ clusters, Nat. Commun. 8 (2017) 170.

[45] Y. Li, W. Ho, K. Lv, B. Zhu, S.C. Lee, Carbon vacancy-induced enhancement of the visible light-driven photocatalytic oxidation of NO over g-C_3N_4 nanosheets, Appl. Surf. Sci. 430 (2018) 380-389.

[46] P. Niu, L.-C. Yin, Y.-Q. Yang, G. Liu, H.-M. Cheng, Increasing the Visible Light Absorption of Graphitic Carbon Nitride (Melon) Photocatalysts by Homogeneous Self-Modification with Nitrogen Vacancies, Adv. Mater. (Weinheim, Ger.) 26 (2014) 8046-8052.

[47] Q. Xiang, J. Yu, M. Jaroniec, Preparation and Enhanced Visible-Light Photocatalytic H_2-Production Activity of Graphene/C_3N_4 Composites, J. Phys. Chem. C 115 (2011) 7355-7363.

[48] F. Wang, P. Chen, Y. Feng, Z. Xie, Y. Liu, Y. Su, Q. Zhang, Y. Wang, K. Yao, W. Lv, G. Liu, Facile synthesis of N-doped carbon dots/g-C3N4 photocatalyst with enhanced visible-light photocatalytic activity for the degradation of indomethacin, Appl. Catal. B 207 (2017) 103-113.

[49] E.S. Da Silva, N.M.M. Moura, A. Coutinho, G. Drazic, B.M.S. Teixeira, N.A. Sobolev, C.G. Silva, M.G.P.M.S. Neves, M. Prieto, J.L. Faria, beta-Cyclodextrin as a Precursor to Holey C-Doped g-C_3N_4 Nanosheets for Photocatalytic Hydrogen Generation, ChemSusChem 11 (2018) 2681-2694.

[50] R.A. Smiley, Phenylene- and Toluenediamines, Wiley‐VCH Verlag GmbH & Co. KGaA2000.

[51] J. Zhang, X. Chen, K. Takanabe, K. Maeda, K. Domen, J.D. Epping, X. Fu, M. Antonietti, X. Wang, Synthesis of a carbon nitride structure for visible-light catalysis by copolymerization, Angew Chem Int Ed Engl 49 (2010) 441-444.

[52] F. Kim, J. Luo, R. Cruz‐Silva, J. Cote Laura, K. Sohn, J. Huang, Self‐Propagating Domino‐like

Reactions in Oxidized Graphite, Adv. Funct. Mater. 20 (2010) 2867-2873.
[53] L. Lin, H. Ou, Y. Zhang, X. Wang, Tri-s-triazine-Based Crystalline Graphitic Carbon Nitrides for Highly Efficient Hydrogen Evolution Photocatalysis, ACS Catal. 6 (2016) 3921-3931.
[54] J. Wen, J. Xie, X. Chen, X. Li, A review on g-C_3N_4-based photocatalysts, Appl. Surf. Sci. 391 (2017) 72-123.
[55] K. Gelderman, L. Lee, S.W. Donne, Flat-Band Potential of a Semiconductor: Using the Mott–Schottky Equation, J. Chem. Educ. 84 (2007) 685.
[56] S.P. Harrington, F. Wang, T.M. Devine, The structure and electronic properties of passive and prepassive films of iron in borate buffer, Electrochim. Acta 55 (2010) 4092-4102.
[57] G. Zhang, C. Ni, L. Liu, G. Zhao, F. Fina, J.T.S. Irvine, Macro-mesoporous resorcinol-formaldehyde polymer resins as amorphous metal-free visible light photocatalysts, J. Mater. Chem. A 3 (2015) 15413-15419.
[58] Y. Cui, J. Huang, X. Fu, X. Wang, Metal-free photocatalytic degradation of 4-chlorophenol in water by mesoporous carbon nitride semiconductors, Catal. Sci. Technol. 2 (2012) 1396-1402.
[59] X. Li, J. Yu, J. Low, Y. Fang, J. Xiao, X. Chen, Engineering heterogeneous semiconductors for solar water splitting, J. Mater. Chem. A 3 (2015) 2485-2534.
[60] J. Liu, Y. Liu, N. Liu, Y. Han, X. Zhang, H. Huang, Y. Lifshitz, S.T. Lee, J. Zhong, Z. Kang, Metal-free efficient photocatalyst for stable visible water splitting via a two-electron pathway, Science 347 (2015) 970-974.
[61] M. Macias-Montero, S. Askari, S. Mitra, C. Rocks, C. Ni, V. Svrcek, P. Connor, P. Maguire, J.T.S. Irvine, D. Mariotti, Energy Band Structure of Device-Grade Silicon Nanocrystals, Nanoscale 8 (2016) 6623-6628.
[62] J.Y. Feng, W.J. Luo, T. Fang, H. Lv, Z.Q. Wang, J. Gao, W.M. Liu, T. Yu, Z.S. Li, Z.G. Zou, Highly Photo-Responsive $LaTiO_2N$ Photoanodes by Improvement of Charge Carrier Transport among Film Particles, Adv. Funct. Mater. 24 (2014) 3535-3542.
[63] W.J. Jiang, Q.S. Ruan, J.J. Xie, X.J. Chen, Y.F. Zhu, J.W. Tang, Oxygen-doped carbon nitride aerogel: A self-supported photocatalyst for solar-to-chemical energy conversion, Appl. Catal. B 236 (2018) 428-435.
[64] X. Wang, K. Maeda, A. Thomas, K. Takanabe, G. Xin, J.M. Carlsson, K. Domen, M. Antonietti, A metal-free polymeric photocatalyst for hydrogen production from water under visible light, Nat. Mater. 8 (2009) 76-80.
[65] X. Xu, C. Randorn, P. Efstathiou, J.T.S. Irvine, A red metallic oxide photocatalyst, Nat. Mater. 11 (2012) 595-598.
[66] L. Li, P.A. Salvador, G.S. Rohrer, Photocatalysts with internal electric fields, Nanoscale 6 (2014) 24-42.
[67] R. Memming, Semiconductor Electrochemistry, Wiley-VCH Verlag GmbH, New York, 2001.
[68] S. Yu, Y. Wang, F. Sun, R. Wang, Y. Zhou, Novel mpg-C_3N_4/TiO_2 nanocomposite photocatalytic membrane reactor for sulfamethoxazole photodegradation, Chem. Eng. J. (Lausanne) 337 (2018) 183-192.
[69] S. Bae, S. Kim, S. Lee, W. Choi, Dye decolorization test for the activity assessment of visible light photocatalysts: Realities and limitations, Catal. Today 224 (2014) 21-28.
[70] W. Cui, J. Li, Y. Sun, H. Wang, G. Jiang, S.C. Lee, F. Dong, Enhancing ROS generation and suppressing toxic intermediate production in photocatalytic NO oxidation on O/Ba co-functionalized amorphous carbon nitride, Appl. Catal. B 237 (2018) 938-946.

[71] Q.L. Yu, H.J.H. Brouwers, Indoor air purification using heterogeneous photocatalytic oxidation. Part I: Experimental study, Appl. Catal. B 92 (2009) 454-461.
[72] M. Kantcheva, A.S. Vakkasoglu, Cobalt supported on zirconia and sulfated zirconia: II. Reactivity of adsorbed NOx compounds toward methane, J. Catal. 223 (2004) 364-371.

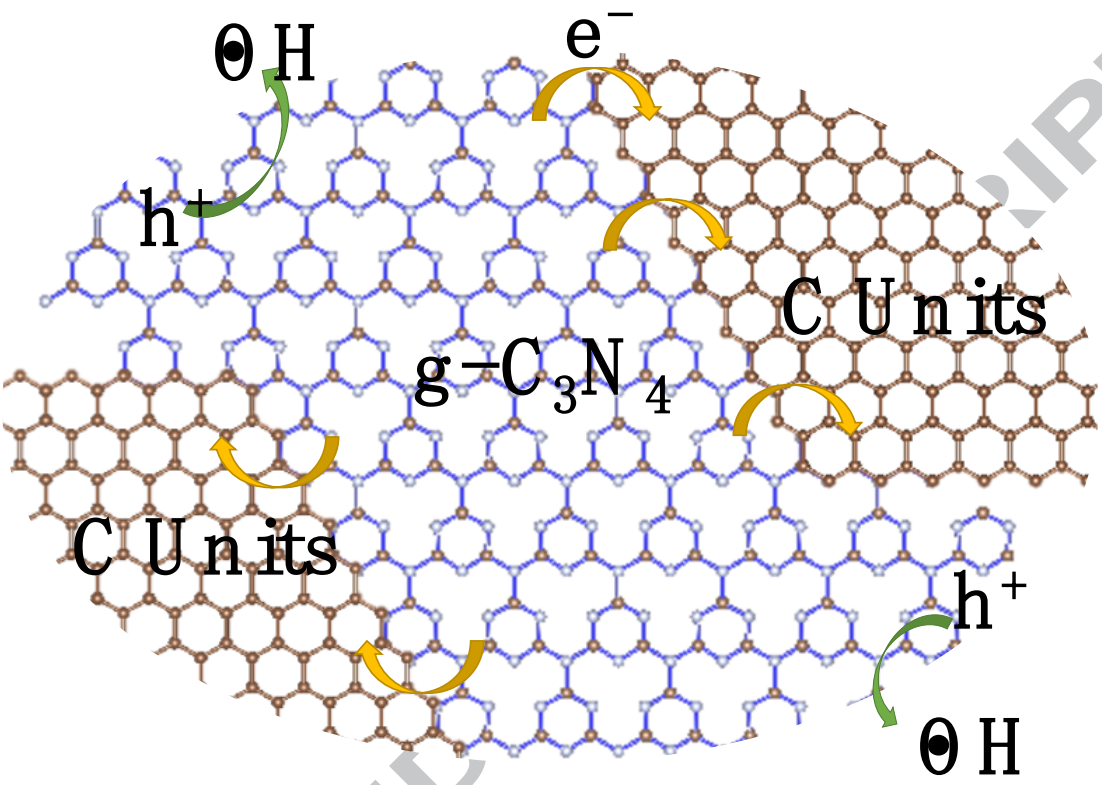

Research Highlights:

- Carbon units modified g-C_3N_4 has been synthesized through m-phenylenediamine doping
- Direct in-plane junction between the carbon units and g-C_3N_4 was observed
- Band edges of g-C_3N_4 was downwards shifted by 1 eV *via* carbon unit doping
- Doped g-C_3N_4 is more efficient in the generation of OH radicals for oxidation process
- *In situ* infrared spectra confirmed the OH group adsorbed on surface of doped g-C_3N_4